Journal of Nuclear Materials 395 (2009) 23–29

Contents lists available at ScienceDirect

Journal of Nuclear Materials

journal homepage: www.elsevier.com/locate/jnucmat

Accelerated testing of HT-9 with zirconia coatings containing gallium using Raman Spectroscopy and XPS

Charles F. Windisch Jr. *, Charles H. Henager Jr., Mark H. Engelhard, Wendy D. Bennett

Pacific Northwest National Laboratory, P.O. Box 999, Richland, WA 99352, United States

ARTICLE INFO

Article history:
Received 18 June 2009
Accepted 23 September 2009

PACS:
81.05.Bx
81.40.Ef
81.65.Kn
81.65.Mq
81.65.Rv
82.80.Gk
82.80.Pv

ABSTRACT

Laser Raman spectroscopy and X-ray photoelectron spectroscopy were used to study the evolution of composition of oxide films in the presence of zirconia coatings on miniature HT-9 alloy specimens subjected to elevated temperature in air. The experiments expanded on previous efforts to develop a quick-screening technique for candidate alloys for cladding materials (HT-9) and actinide-based mixed oxide fuel mixtures (represented by the zirconia coating) by investigating the effect of both coating composition and annealing conditions on the high temperature reactions. In particular, the presence of the element Ga (a potential impurity in mixed oxide fuel) in the initial zirconia coating was found to accelerate the rate of oxide growth relative to that of yttria-stabilized zirconia studied previously. In addition, HT-9 samples that were subjected to different annealing conditions gave different results. The results suggest that the presence of Ga in a mixed oxide fuel will enhance the oxidation of HT-9 cladding under the conditions of this study, although the extent of enhancement is influenced by the type of annealing previously applied to the cladding material. Due to the multi-component layered structure of the oxidation products discovered in this fuel-cladding combination, it appears unlikely that Raman spectroscopy would be applicable as a stand-alone technique for the intended quick-screening approach to all but the simplest systems. Other techniques with better depth resolution, such as photoelectron spectroscopy, are required to follow the changes in composition of individual layers as they evolve during the oxidation process.

1. Introduction

As discussed in our previous paper [1], a knowledge of the chemical interactions of oxide fuel with the cladding material is critical to planning an efficient path forward in the development of both improved mixed oxide (MOX) fuel and cladding compositions for the advanced recycle reactors (ARR). This work continues our efforts to develop an approach for relatively rapid screening of new materials, based primarily on laser Raman spectroscopy (LRS). As envisioned, LRS would be applied as a stand-alone technique to study reaction kinetics in real time at elevated temperature using a spectroscopy hot stage. However, in this early stage of development, the technique was applied to samples first held at elevated temperature and then quenched for subsequent ex situ analysis. The analysis was also supported by X-ray photoelectron spectroscopy (XPS), which is critical to determining composition information as a function of depth. It was hoped that a more comprehensive database of combined LRS–XPS would lead to a sufficiently unambiguous relationship between data from the two techniques (and an accompanying understanding of the depth/composition relationship of components) that LRS could be used independently for the rapid screening of materials.

Similar to our previous work, miniature 3-mm diameter disks of HT-9 coated with surrogate zirconia were used to simulate cladding in contact with an oxide fuel. The zirconia coatings used in the present work, however, were doped with Ga, a known impurity in MOX fuel [2–7]. Residual Ga in MOX at approximately 1% by weight is of great concern due to issues of liquid metal embrittlement with cladding [8–12] and with regard to fuel performance [2–7]. Oxidation may not be as severe with ferritic steel cladding compared to zirconium alloy cladding as proposed for some ARR systems, but the fuel performance issue still holds. Our interest was in determining the influence of the Ga within the zirconia coating on the oxidation properties of the HT-9 at elevated temperatures. Two sets of HT-9 samples were tested, distinguished by different annealing temperatures used during fabrication. Subsequent heat treatments were then applied in "accelerated test" under conditions similar to those determined previously [1] to produce a sufficient amount of oxidation products to give Raman spectra with adequate signal-to-noise. Both LRS and XPS were applied to these samples.

* Corresponding author. Tel.: +1 509 375 6538; fax: +1 509 375 2186.
E-mail address: cf.windisch@pnl.gov (C.F. Windisch).

0022-3115/$ - see front matter © 2009 Elsevier B.V. All rights reserved.
doi:10.1016/j.jnucmat.2009.09.011

2. Experimental procedure

Miniature, 3-mm diameter, HT-9 samples were "punched" from a 0.2-mm thick sheet of material obtained from a lot of FFTF Core Demonstration heat that had been rolled into 0.25-mm thick strips and annealed in Ti-gettered evacuated quartz ampoules under two sets of conditions followed by air cooling. The bulk composition of the HT-9 samples as reported by the manufacturer is given in Table 1 and the annealing conditions are provided in Table 2. The latter were chosen to produce a tempered martensite structure [13], verified in our samples for both annealing conditions by using optical metallography (Fig. 1). Tensile data obtained on miniature tensile specimens [14] (5-mm gage length, 1.2 mm × 0.25 mm gage cross-section) indicated substantial softening following the 86.4-ks temper at 1023 K compared to 3.6 ks at 923 K (Fig. 2). Prior to applying coatings or obtaining any spectra, the miniature samples were ground with 600-grit SiC, polished to a 1-micron diamond finish, rinsed with water, and then ultrasonically cleaned in acetone.

Some samples were tested without any coating. Others were first coated with a thin film of Ga-doped zirconium oxide (GZO) containing approximately 5 at.% Ga deposited by DC reactive magnetron sputtering using conditions reported previously [1] with a starting target material comprised of a Zr/Ga (wt.% ratio = 90/10) alloy. Both uncoated and coated samples were heated at 923 K for various times up to 28.8 ks using an open-air electric furnace, then cooled to room temperature and analyzed with LRS and XPS. This heating step, hereafter referred to as the "heat treatment" to distinguish it from the annealing process, is the accelerated test that is the primary focus of this work. The conditions for this test were chosen because they previously were shown [1] to give sufficient amount of oxidation products so they could be identified with LRS. Spectral acquisition parameters for both techniques were also the same as reported in our previous paper [1]. In particular, Raman spectra were acquired in the backscatter configuration using a Spex (Edison, NJ) Model 1877 spectrometer equipped with a Princeton Instruments (Trenton, NJ) liquid nitrogen cooled charge-coupled detector (LN/CCD) and the 488.0-nm line of a Coherent (Santa Clara, CA) Innova 307 Ar^+ ion laser for excitation. The slit width was 400 μm and the exposure time was 1000 s for all samples. The estimated uncertainty of the peak frequencies was ± 1 cm^{-1}. XPS measurements were performed using a Physical Electronics (Chanhassen, MN) Quantum 2000 Scanning ESCA Microprobe equipped with a focused monochromatic Al Kα X-rays (1486.7 eV) source and a spherical section analyzer. Sample sputtering was performed using 2 kV Ar^+ ions rastered over a 2 mm × 2 mm area of the specimen at a rate of approximately 0.13 nm s^{-1}, based on comparison to a known SiO_2 reference material. During a sputter-depth profile study, XPS spectra were collected after arbitrary sputtering time increments (cycles). Sputter depth can therefore be expressed in terms of the number of sputtering cycles or time of sputtering or, by using the SiO_2 reference, estimated in geometric units.

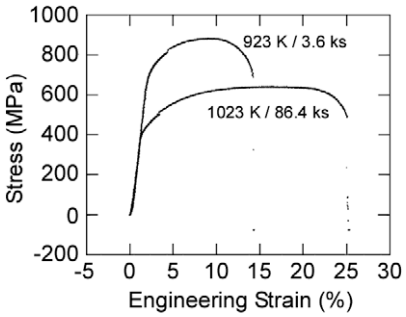

Fig. 2. Engineering stress–strain curves at ambient temperature from miniature tensile tests of tempered martensitic steel (HT-9).

Table 1
HT-9 composition.

Material	Cr	C	Si	Mn	W	V	Mo	Ni	Fe
HT-9	11.8	0.21	0.29	0.53	0.52	0.33	1.06	0.6	Balance

Table 2
HT-9 annealing conditions.

Sample name	Annealing conditions[a]
HT9-229-1	1323 K for 600 s followed by 923 K for 3.6 ks
HT9-229-3	1323 K for 600 s followed by 1023 K for 86.4 ks

[a] Both samples were annealed in Ti-gettered evacuated quartz ampoules followed by air cooling.

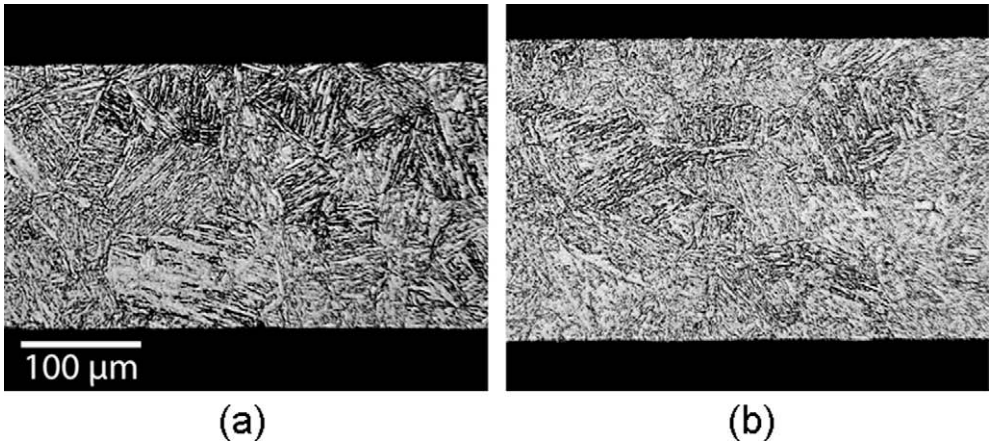

Fig. 1. Optical micrographs of polished sections of tempered martensitic structure in HT-9 materials following annealing as indicated in Table 2: (a) 923 K for 3.6 ks and (b) 1023 K for 86.4 ks.

3. Results and discussion

3.1. Before heat treatment

After polishing but prior to subsequent heat treatment, samples of HT9-229-1 and HT9-229-3 that were not coated with GZO were shown to be passivated with thin oxide films. Depth profiling using XPS gave film thicknesses of approximately 5 nm and 10 nm for HT9-229-1 and HT9-229-3, respectively, and showed the principal components of the film were iron oxide near the surface and a mixed metal oxide containing Fe with increasing concentration of Cr closer to the metal/metal oxide interface. Unfortunately, the passive films were too thin to give sufficient scattering for characterization with LRS.

As shown in Fig. 3, the XPS depth profile of a HT9-229-1 sample that had been coated with GZO showed that the coating was 80–100 nm thick. The GZO coating on a HT9-229-3 sample was similarly thick. Depth profiling (Fig. 3) also showed that the GZO coatings on both alloys contained ca. 5 at.% Ga and no detectable amount of Fe prior to heat treatment. Some of the Zr in the GZO coating was in reduced form (valence <+4) as shown by the presence of a $Zr3d_{5/2}$ peak at approximately 179.7 eV in Fig. 4. The $Zr3d_{5/2}$ peak for zero-valent Zr is reported at 178.9 eV, compared to ZrO_2 (182.2 eV) [15]. The amount of reduced Zr was essentially constant over the full thickness of the coating (to 90 nm or cycle 13 in Fig. 4). Right at the GZO/metal interface (cycle 14), the Zr was mainly in the reduced form. Gallium was also found to be reduced over the same depth as shown by the position of the $Ga2p_{3/2}$ peak in Fig. 5. The $Ga2p_{3/2}$ peak in Ga and Ga_2O_3 is reported at binding energies of 1116.7 eV and 1117.8 eV [15], respectively. The first two cycles of sputtering, however, indicated that Ga was oxidized right at the GZO surface. While data in Figs. 4 and 5 are for HT9-229-1, exactly the same trends in Zr and Ga were observed in the spectra of HT9-229-3. Notice also that the depth profile in Fig. 3 shows a slight deficiency in oxygen relative to stoichiometric ZrO_2, except right at the surface where there is excess oxygen. Given that Ga in the film is reduced, the deficiency in oxygen is consistent with the presence of a significant quantity of reduced Zr in the film. The presence of reduced Zr is also consistent with our previous findings on HT-9 coated with yttria-stabilized zirconia (YSZ). The sputter deposition process resulted in a small amount of uniformly distributed reduced-valence Zr in all of the zirconia films studied to date, despite the oxidizing conditions employed in the deposition process.

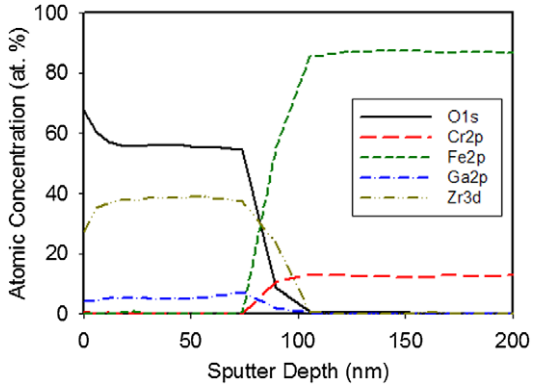

Fig. 3. XPS depth profile for GZO-coated HT9-229-1, prior to heat treatment at 923 K in air. Based on comparison to a known SiO_2 reference material, the sputter rate was approximately 0.13 nm s^{-1}.

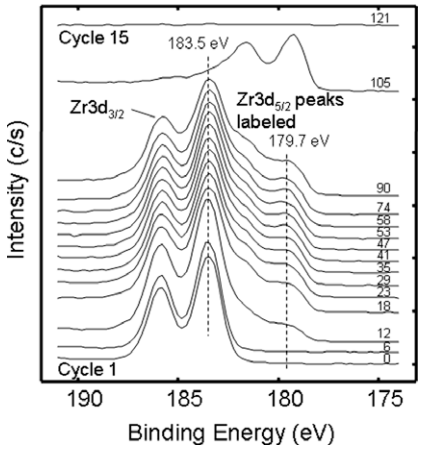

Fig. 4. Variation of XPS $Zr3d_{5/2}$ peaks with depth during the first 15 sputtering cycles for HT9-229-1 sample with GZO coating, prior to heat treatment at 923 K in air. The sputter depth in nm for each spectrum is indicated.

3.2. After heat treatment

Raman spectra acquired for HT9-229-1 and HT9-229-3 (both with and without the GZO coating) after 7.2 ks of heating at 923 K in air are shown in Figs. 6 and 7. Clearly, the oxide films have grown in all samples to the point of being easily detected with LRS. The band at 412 cm^{-1}, which is always accompanied by prominent

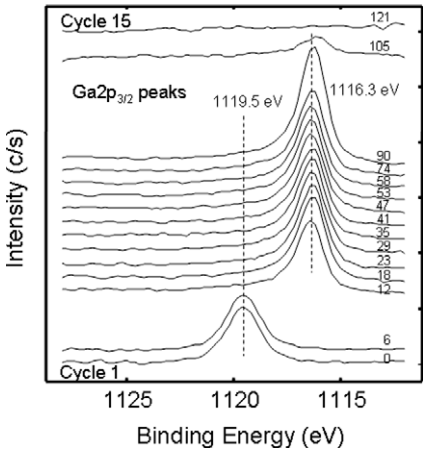

Fig. 5. Variation of XPS $Ga2p_{3/2}$ peaks with depth during the first 15 sputtering cycles for HT9-229-1 sample with GZO coating, prior to heat treatment at 923 K in air.

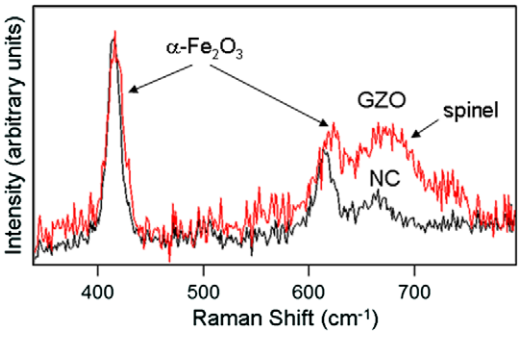

Fig. 6. Raman spectra of HT9-229-1 with no coating (NC) and coated with GZO (GZO), after heating at 923 K in air for 7.2 ks. Spectra are normalized to the peak at 412 cm^{-1} arising from α-Fe_2O_3.

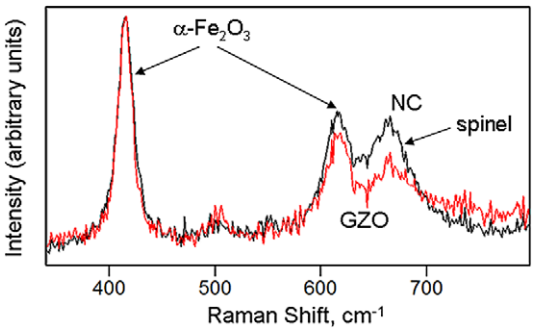

Fig. 7. Raman spectra of HT9-229-3 with no coating (NC) and coated with GZO (GZO), after heating at 923 K in air for 7.2 ks. Spectra are normalized to the peak at 412 cm^{-1} arising from α-Fe_2O_3.

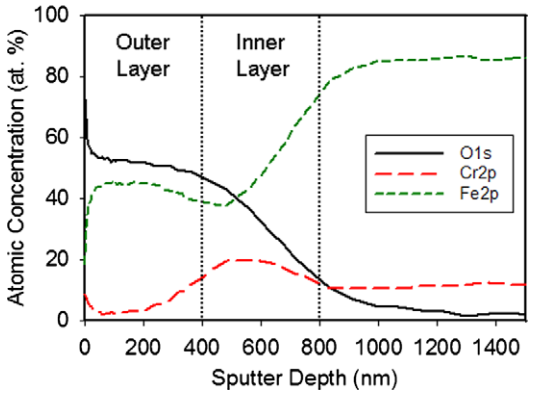

Fig. 8. XPS depth profile for uncoated HT9-229-1, after heating in air at 923 K for 7.2 ks.

bands at 297 cm^{-1} (not shown in these spectra) and 612 cm^{-1} (shown), is indicative of α-Fe2O3 (hematite) [16,17]. The broad band around 685 cm^{-1} is attributed to the spinel oxide(s) Fe_2CrO_4 and/or $FeCr_2O_4$ [1,16]. As shown in Figs. 6 and 7, both α-Fe_2O_3 and an oxide spinel form on HT9-229-1 and HT-229-3 during the 7.2-ks heating. Unlike our previous work on unpolished samples with and without YSZ films, no evidence for Cr_2O_3 was found (absence of Raman peak at 549 cm^{-1}). In the case of HT9-229-1, when the spectra were normalized to the α-Fe_2O_3 band at 412 cm^{-1}, the intensity of the oxide spinel band was greater when the GZO coating was present than without the coating. For HT9-229-3, the behavior was opposite: the intensity of the oxide spinel band was less when the GZO coating was present than without the coating. Raman spectra were also collected on both HT9-229-1 and HT-229-3 after heating in air at 923 K for up to 28.8 ks and these were found to be remarkably similar to those in Figs. 6 and 7, following the same trends with only minor differences in relative intensities.

XPS depth profiling of the HT9-229-1 (Fig. 8) and HT9-229-3 (Fig. 9) samples with no GZO coating after heat treatment for 7.2 ks revealed an oxidation product containing Fe- and Fe + Cr-rich layers, consistent with the presence of α-Fe_2O_3 and the oxide spinel identified by LRS. The outer layer, apparently mostly α-Fe_2O_3, was about 400 nm thick in the case of HT9-229-1 and 60 nm thick for HT9-229-3. The thickness of the inner layer was comparable to that of the α-Fe_2O_3 in both cases and, given the mixture of Fe and Cr in the XPS as well as the presence of oxide spinel in the Raman spectra, is mostly a mixed Fe–Cr oxide spinel. The layered structure and its composition are consistent with other studies [18] on high temperature oxidation of steels that reported duplex films with α-Fe_2O_3 on the outside and Cr-containing oxides closer to the metal/metal oxide interface.

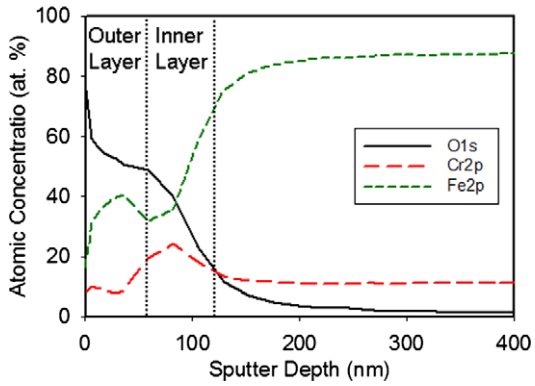

Fig. 9. XPS depth profile for uncoated HT9-229-3, after heating in air at 923 K for 7.2 ks.

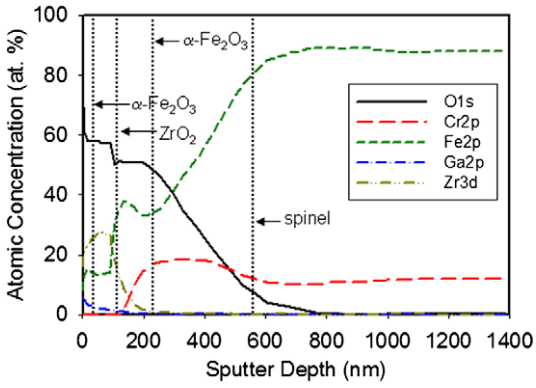

Fig. 10. XPS depth profile for GZO-coated HT9-229-1, after heating in air at 923 K for 7.2 ks.

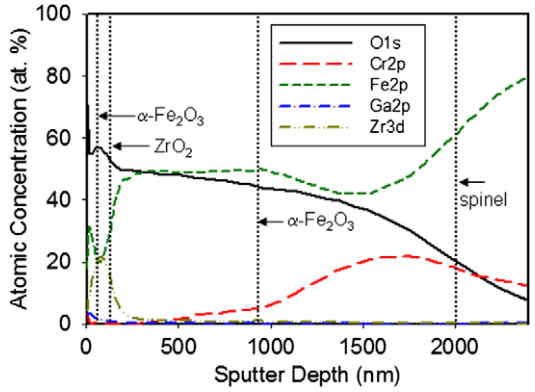

Fig. 11. XPS depth profile for GZO-coated HT9-229-3, after heating in air at 923 K for 7.2 ks.

XPS depth profiling of the GZO-coated samples that had been heat treated (Figs. 10 and 11) showed a slightly refined Zr profile, with no significant change in thickness of the GZO but noticeably rounded boundaries, and the formation of significant amount of oxidation products on top of, and especially under, the GZO coating.

The presence of a significant amount of Fe is noted in the GZO coating for both HT9-229-1 (Fig. 10) and HT9-229-3 (Fig. 11) and also on top of the GZO coating, i.e. in a ca. 50-nm thick layer of, presumably, α-Fe_2O_3. The oxide under the GZO coating is remarkably thick and appears to be a duplex-layer composed of α-Fe_2O_3 near

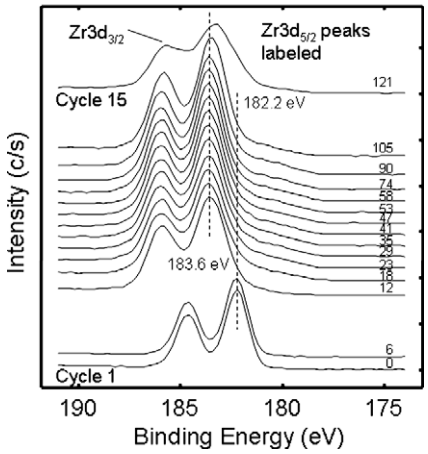

Fig. 12. Variation of XPS $Zr3d_{5/2}$ peaks with depth during the first 15 sputtering cycles for HT9-229-1 sample with GZO coating, after heating in air at 923 K for 7.2 ks.

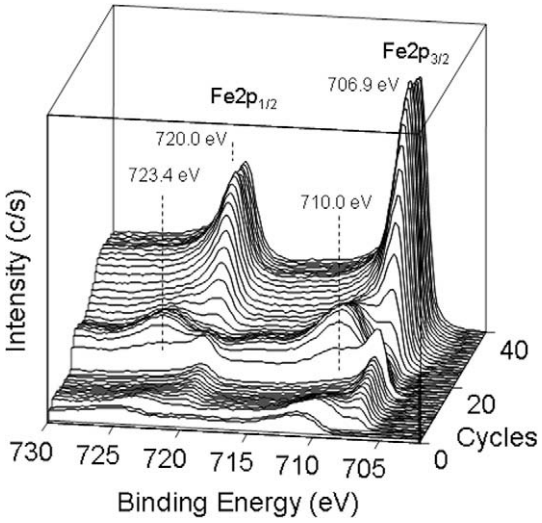

Fig. 13. Variation of XPS $Fe2p_{3/2}$ peaks with depth during the first 40 sputtering cycles for HT9-229-1 sample with GZO coating, after heating in air at 923 K for 7.2 ks. The sputter depth per cycle was different between cycle intervals 1–20 and 21–40, although it was maintained nearly the same within each interval. For reference, the accumulated sputter depth was 199 nm at 20 cycles and 1230 nm at 40 cycles.

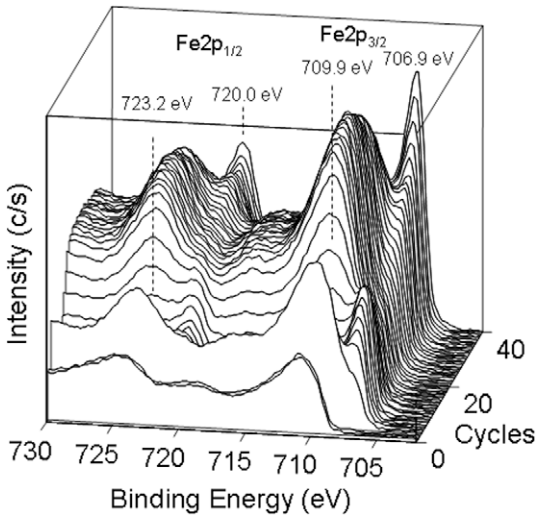

Fig. 14. Variation of XPS $Fe2p_{3/2}$ peaks with depth during the first 40 sputtering cycles for HT9-229-3 sample with GZO coating, after heating in air at 923 K for 7.2 ks. The sputter depth per cycle was different between cycle intervals 1–20 and 21–40, although it was maintained nearly the same within each interval. For reference, the accumulated sputter depth was 367 nm at 20 cycles and 1690 nm at 40 cycles.

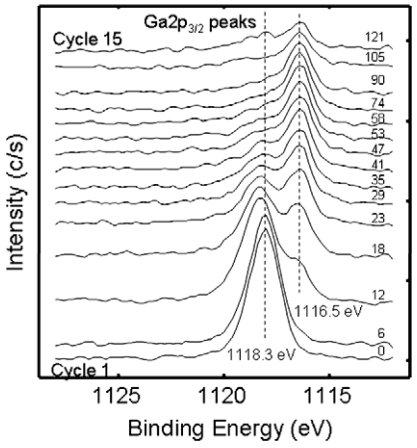

Fig. 15. Variation of XPS $Ga2p_{3/2}$ peaks with depth during the first 15 sputtering cycles for HT9-229-1 sample with GZO coating, after heating in air at 923 K for 7.2 ks.

the GZO coating and a mixed Fe–Cr oxide spinel underneath. The thickness of the buried duplex layer is about 455 nm for HT9-229-1 (130 nm α-Fe_2O_3 + 325 nm spinel oxide), compared to about 1.9 μm for HT-220–3 (750 nm α-Fe_2O_3 + 1100 nm spinel oxide). Also, the depth profiles in Figs. 10 and 11 indicate that Ga has been lost from the GZO on both alloys, particularly deeper within the GZO coating and especially in the case of HT9-229-3.

As shown in Fig. 12, virtually none of the reduced Zr originally in the film remains in the lower valence state (peak at 179.7 eV is absent) after 7.2 ks heating in air and, as shown in the 3-D plots in Figs. 13 and 14, the Fe that winds up in the GZO coating as a result of heat treatment is in reduced form (peak at 706.9 eV between cycles 0 and 15). This result, which occurred for both HT9-229-1 and HT-229-3, is similar to the behavior of the YSZ films (which also initially contained small amounts of reduced Zr) reported previously [1] and is explained by the following single replacement reaction during heating:

$$4\ Fe_2CrO_4 + Zr \rightarrow\ 2Fe + 2\alpha\text{-}Fe_2O_3 + 2FeCr_2O_4 + ZrO_2 \qquad (1)$$

We believe that the same reaction occurs within the GZO coating in the present study during heating. The $Fe2p_{3/2}$ region in Figs. 13 and 14 illustrates the varying oxidation state of Fe as a function of film thickness that is consistent with (a) a thin layer of α-Fe_2O_3 right at the surface (peak at ca. 710.0 eV in the first few cycles), (b) the presence of reduced Fe within the GZO coating (peak at 706.9 eV up to cycle 15 as discussed previously), and (c) a thick buried iron-containing oxide layer underneath (peak at ca. 710.0 eV in cycles after 15). The difference in thickness of the buried oxide layer for HT9-229-1 and HT9-229-3 is also apparent in the figures. As shown in Fig. 15, the $Ga3p_{3/2}$ region indicates that the loss of Ga in the GZO coating (see the depth profiles in Figs. 10 and 11) is accompanied by an increase in oxidation state of the remaining Ga (peak at 1118.3 eV). Similar results for the Ga in the GZO coating were observed for both HT9-229-1 and HT9-229-3, although the $Ga3p_{3/2}$ peaks for HT9-229-3 were weaker because of the smaller amount of Ga remaining in the coating (Fig. 11).

3.3. Role of gallium

The above results indicate that Ga, when present in a reduced valence state, lowers the passivity of coatings on HT-9 significantly during heating at 923 K compared to YSZ films studied previously [1]. Moreover, the annealing conditions of the HT-9 prior to coating appear to be important, with higher annealing temperature and time (HT9-229-3) enhancing oxidation when the GZO coating was present.

During heat treatment, a significant portion of the Ga migrated out of the GZO coating. Given that Ga melts at 303 K, it is possible that the transport is toward the surface via the liquid phase and material loss is explained by evaporation. However, it is also possible that the Ga migrated toward the metal/metal oxide interface and participated directly in oxidation reactions that explain the thick buried layer of corrosion products. The buried oxides, which included both α-Fe_2O_3 and a Fe–Cr oxide spinel, approached or exceeded a micron in thickness after 7.2 ks and were significantly thicker in the case of HT9-229-3. Some of the Ga also remained in the film in an oxidized state, either incorporated in the GZO lattice or as a separate gallium oxide phase.

The migration of Ga toward the metal/metal oxide interface would be consistent with previous reports on the corrosion of stainless steels in contact with both liquid gallium [19,20] and gallium oxides [21]. However, what happens once the Ga is transported to the interface is not certain from this study. Based on the cited work, the Ga may penetrate the metal along grain boundaries and cause intergranular corrosion. This means that the Ga could serve two roles: lowering the passivity of the film and (subsequent to migration) enhancing intergranular corrosion of the base metal. The influence of annealing conditions on oxide growth and composition (generally thicker oxide films were observed with higher-temperature, longer-time, annealing) might also be partly explained by the impact of different annealing conditions on the Cr distribution in the alloy, especially along grain boundaries, although this is speculation in the absence of higher-resolution transmission electron microscopic measurements. The bulk concentration of the Cr does not appear to be influenced significantly by the different annealing conditions. The Cr/Fe at.% ratio in the bulk metal calculated from XPS depth profiles varies between 0.13 to 0.17 for all samples with no apparent correlation with annealing conditions, coating application, or subsequent heat treatment.

3.4. Interpretation of Raman spectra

Re-examination of Figs. 6 and 7 in light of the XPS depth profiling data leads to an important consideration concerning the use of LRS for the screening of cladding and oxide fuel materials in an accelerated test, which was the primary motivation for this work. When the spectra were normalized to the 412 cm^{-1} band from α-Fe_2O_3 for each of the two sets of HT-9 samples, it appears that more spinel oxide (broad peak at ca. 685 cm^{-1}) forms when HT9-229-1 is coated with GZO (compared to the uncoated sample) whereas less spinel forms when HT9-229-3 is coated with GZO (compared to the uncoated sample). This could lead to the erroneous conclusion that the GZO coating is more protective for HT9-229-3 than for HT9-229-1. As shown in the XPS depth profiles in Figs. 8–11, HT9-229-1 actually oxidized to a slightly less extent when the coating was present (compare Figs. 8 and 10), compared to HT9-229-3 which oxidized by over a magnitude more when the coating was present (compare Figs. 9 and 11). Moreover, the amount of oxidation products under the GZO coating was significantly greater for HT9-229-3 when the coating was present than without it, which appears to be directly opposite the behavior suggested by the Raman spectra in Fig. 7.

The reason for the apparent inconsistency between the LRS and XPS data highlights the challenge of using Raman spectra quantitatively when a true reference intensity is unavailable. In our work, the Raman spectra were normalized with respect to the 412 cm^{-1} band arising from α-Fe_2O_3. This peak was selected as a reference peak because it was strong in all of the spectra and relatively narrow. It is not a true reference however, because the amount of α-Fe_2O_3 varied from sample to sample and its distribution as a function of depth also varied. Both of these characteristics should influence the intensities of the α-Fe_2O_3 peaks and their contribution was not distinguished by LRS. Rather, XPS was used to discern them. The alternative approach of not scaling the Raman intensities at all is also fraught with difficulty since the absolute intensities of all peaks in a spectrum are subject to variations in sample position when a series of samples are studied, as they were in this study. One cannot quantify, for example, the relative amount of spinel oxide from sample to sample by comparing the absolute intensity of the 685 cm^{-1} peak. Without further consideration of the scattering properties of each sample, our best explanation for the Raman spectra is that the large quantity of α-Fe_2O_3 formed on HT9-229-3, both on top of and under the GZO coating, makes the relative amount of spinel oxide look smaller since it is buried significantly deeper within the oxide layer under the GZO coating. In conclusion, while the Raman spectra serve an important purpose in identifying the composition of the oxides that comprise the oxidation products in all of the HT-9 samples studied in this work, the complex layered structure of the oxides, particularly on samples with the GZO coating, made it difficult to analyze the spectra quantitatively without the supporting information from XPS.

4. Conclusions

Raman spectra acquired on HT-9 samples, with and without a Ga-containing zirconia coating, showed that heat treatment at 923 K in air produced oxidation products both on top of the coating and under it. The amount of oxidation products was similar to or greater than that measured on uncoated samples and significantly greater than observed previously on samples coated with YSZ. The oxidation products were layered and composed mainly of α-Fe_2O_3 and Fe–Cr oxide spinel. The spinel oxide formed under the zirconia coating and closer to the metal than the α-Fe_2O_3. Reduced Zr in the coating was found to oxidize during heat treatment in a single replacement reaction that also resulted in the formation of lower-valence Fe in the film. Coincidently, the Ga was found to migrate out of the coating and oxidize. In light of our previous work on HT-9 coated with YSZ, we are led to the conclusion that the presence of Ga in the zirconia coating makes it significantly less protective. In regard to our assessment of the materials screening approach, using laser Raman spectroscopy alone is not recommended if there is suspicion that the oxidation products form in layers. The technique needs to be combined with other methods that allow for depth profiling of composition. For systems that prove to be relatively simple in composition and structure, it is possible that sufficient calibration with XPS data could enable Raman spectroscopy as a stand-alone screening tool. However, the complexity of the behavior of samples in this study indicates that one should be careful in applying this approach on all systems, even those that have been well-characterized using other techniques.

Acknowledgment

This research was sponsored by the Sustainable Nuclear Power Initiative at the Pacific Northwest National Laboratory (PNNL) under the Laboratory Directed Research and Development program. PNNL is operated by Battelle Memorial Institute for the US Depart-

ment of Energy under Contract No. DE-AC06-76RLO1830. A portion of the research was performed using EMSL, a national science user facility sponsored by the Department of Energy's Office of Biological and Environmental Research located at PNNL.

References

[1] C.F. Windisch Jr., C.H. Henager Jr., M.H. Engelhard, W.D. Bennett, J. Nucl. Mater. 383 (2009) 237.
[2] E.A. Bluhm, K.D. Abney, S. Balkey, J.C. Brock, F. Coriz, J.T. Dyke, D.J. Garcia, B.J. Griego, B.T. Martinez, D. Martinez, J.R. Martinez, Y.A. Martinez, L. Morgan, J.D. Roybal, J.A. Valdez, K.B. Ramsy, B.K. Bluhm, C.D. Martinez, M.M. Valdez, Sep. Sci. Technol. 40 (2005) 281.
[3] D.F. Williams, G.D. Del Cul, L.M. Toth, E.D. Collins, Nucl. Technol. 136 (2001) 367.
[4] J.R. Schoonover, A. Saab, J.S. Bridgewater, G.J. Havrilla, C.T. Zugates, P.J. Treado, Appl. Spectrosc. 54 (2000) 1362.
[5] D.G. Kolman, M.E. Griego, C.A. James, O.P. Butt, J. Nucl. Mater. 282 (2000) 245.
[6] C.G. Worley, G.J. Havrilla, Anal. Chem. 70 (1998) 2957.
[7] T.M. Besmann, J. Am. Chem. Soc. 81 (1998) 3071.
[8] D.F. Wilson, J.r. DiStefano, J.P. Strizak, J.F. King, E.T. Manneschmidt, Interactions of Zircaloy Cladding with Gallium: Final Report, Oak Ridge National Laboratory Technical Report No. ORNLTM-13684, Oak Ridge, TN, September 1998.
[9] P.H. Au-Yeung, J.T. Lukowski, L.A. Heldt, C.L. White, Scr. Metall. 24 (1990) 95.
[10] M. K. West, Gallium Interactions with Zircaloy, Amarillo National Resource Center for Plutonium Technical Report No. ANRCP-1999-2, Amarillo, TX, January 1999.
[11] D.G. Kolman, M.E. Griego, C.A. James, D.P. Butt, J. Nucl. Mater. 282 (2000) 245.
[12] R. R. Hart, J. Rennie, K. Aucoin, M. West, K. Unl, and C. Rios-Martinez, Gallium Interactions with Zircaloy Cladding, Amarillo National Resource Center for Plutonium Report No. ANRCP-1998-5, Amarillo, TX, 1998.
[13] P. Hosemann, C. Vieh, R.R. Greco, S. Kabra, J.A. Valdez, M.J. Cappiello, S.A. Maloy, J. Nucl. Mater. 389 (2009) 239.
[14] H. Kurishita, H. Kayano, M. Narui, A. Kimura, M.L. Hamilton, D.S. Gelles, J. Nucl. Mater. 212 (1994) 730.
[15] J. F. Moulder, W. F. Stickle, P.E. Sobol, and K.D. Bomben, Handbook of X-ray Photoelectron Spectroscopy, Physical Electronics, Inc., Eden Prairie, MN, 1995.
[16] S.C. Tjong, Mater. Res. Bull. 18 (1983) 157.
[17] D.J. Gardiner, C.J. Littleton, K.M. Thomas, K.N. Strafford, Oxid. Met. 27 (1987) 57.
[18] N. Birks, G. Meier, F. Pettit, High Temperature Oxidation of Metals, second ed., Cambridge University Press, Cambridge, UK, 2006.
[19] K.A. Narh, V.P. Dwivedi, M.M. Graw, A. Stana, W.-Y. Shih, J. Mater. Sci. 33 (1998) 329.
[20] F. Barbier, J. Blanc, J. Mater. Res. 14 (1999) 737.
[21] D.G. Kolman, T.N. Taylor, Y.S. Park, M. Stan, D.P. Butt, C.J. Maggiore, J.R. Tesmer, G.J. Havrilla, Oxid. Met. 55 (2001) 437.